

Residual Degradation Learning Unfolding Framework with Mixing Priors across Spectral and Spatial for Compressive Spectral Imaging

Yubo Dong Dahua Gao* Tian Qiu Yuyan Li Minxi Yang Guangming Shi
School of Artificial Intelligence, Xidian University

{ybdong, tianqiu, liyuyan, mxyang}@stu.xidian.edu.cn {dhgao, gmshi}@xidian.edu.cn

Abstract

To acquire a snapshot spectral image, coded aperture snapshot spectral imaging (CASSI) is proposed. A core problem of the CASSI system is to recover the reliable and fine underlying 3D spectral cube from the 2D measurement. By alternately solving a data subproblem and a prior subproblem, deep unfolding methods achieve good performance. However, in the data subproblem, the used sensing matrix is ill-suited for the real degradation process due to the device errors caused by phase aberration, distortion; in the prior subproblem, it is important to design a suitable model to jointly exploit both spatial and spectral priors. In this paper, we propose a Residual Degradation Learning Unfolding Framework (RDLUF), which bridges the gap between the sensing matrix and the degradation process. Moreover, a Mix S^2 Transformer is designed via mixing priors across spectral and spatial to strengthen the spectral-spatial representation capability. Finally, plugging the Mix S^2 Transformer into the RDLUF leads to an end-to-end trainable neural network RDLUF-Mix S^2 . Experimental results establish the superior performance of the proposed method over existing ones. Code is available: https://github.com/ShawnDong98/RDLUF_MixS2

1. Introduction

With the application of coded aperture snapshot spectral imaging (CASSI) [1, 22, 30, 34], it has become feasible to acquire a spectral image using a coded aperture and dispersive elements to modulate the spectral scene. By capturing a multiplexed 2D projection of the 3D data cube, CASSI technique provides an efficient approach for acquiring spectral data. Nonetheless, the reconstruction of an accurate and detailed 3D hyperspectral image (HSI) cube from the 2D measurements poses a fundamental challenge for the CASSI system.

Based on CASSI, various reconstruction techniques have

This work was supported by the National Key Research and Development Program of China (No. 2019YFA0706604), the Natural Science Foundation (NSF) of China (Nos. 61976169, 62293483).

* Corresponding author.

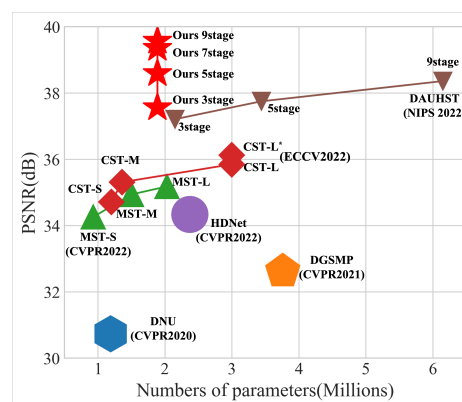


Figure 1. Comparison of PSNR-Parameters with previous HSI reconstruction methods. The PSNR (in dB) is plotted on the vertical axis, while memory cost parameters are represented on the horizontal axis. Our proposed Residual Degradation Learning Unfolding Framework with Mixing priors across Spatial and Spectral (RDLUF-Mix S^2) Transformers outperforms previous methods while requiring fewer parameters.

been developed to reconstruct the 3D HSI cube from 2D measurements. These methods range from model-based techniques [15, 17, 18, 30, 33, 35, 38, 43], to end-to-end approaches [5, 13, 16, 22, 23], and deep unfolding methods [14, 31, 32]. Among them, deep unfolding methods have demonstrated superior performance by transferring conventional iterative optimization algorithms into a series of deep neural network (DNN) blocks. Typically, the deep unfolding methods tackle a data subproblem and a prior subproblem iteratively.

The data subproblem is highly related to the degradation process. The ways to acquire the degradation matrix in the data subproblem can be classified into two types, the first directly uses the sensing matrix as the degradation matrix [19, 21, 32] and the other learns the degradation matrix using a neural network [14, 24, 44]. However, since the sensing matrix is obtained from the equidistant lasers of different wavelengths on the sensor, it cannot reflect the device errors caused by phase aberration, distortion and alignment of the continuous spectrum. Thus, the earlier kind does not take into account the gap between the sensing matrix and

the degradation process. In the latter type, directly modeling the degradation process is challenging. Considering the challenge of optimizing the original, unreferenced mapping, it is preferable to focus on optimizing the residual mapping. Therefore, we explicitly model the degradation process as residual learning with reference to the sensing matrix.

For the prior subproblem, a denoiser is trained to represent the regularization term as a denoising problem in an implicit manner, typically implemented as an end-to-end neural network. Recently, Spectral-wise Multi-head Self-Attention (S-MSA) has been introduced to model long-range dependency in the spectral dimension. However, S-MSA may neglect spatial information that is crucial for generating high-quality HSI images, due to its implicit modeling of spatial dependency. To this end, the integration of Convolutional Neural Networks (CNNs) with S-MSA can provide an ideal solution as CNNs have the inductive bias of modeling local similarity, thus enhancing the spatial modeling capabilities of S-MSA. To achieve this, we propose a multiscale convolution branch that processes visual information at multiple scales and then aggregates it to enable simultaneous feature abstraction from different scales, thereby capturing more textures and details.

In this paper, we first unfold the Proximal Gradient Descent (PGD) algorithm under the framework of maximum a posteriori theory for HSI reconstruction. Then, we integrate the residual degradation learning strategy into the data subproblem of PGD, which bridges the gap between the sensing matrix and the degradation process, leading to our Residual Degradation Learning Unfolding Framework (RDLUF). Secondly, a multiscale convolution called Lightweight Inception is combined with spectral self-attention in a parallel design to address the problem of weak spatial modeling ability of S-MSA. To provide complementary clues in the spectral and spatial branches, we propose a bi-directional interaction across branches, which enhance the modeling ability in spectral and spatial dimensions respectively, resulting in our Mixing priors across Spatial and Spectral (Mix S^2) Transformer. Finally, plugging the Mix S^2 Transformer into the RDLUF as the denoiser of the prior subproblem leads to an end-to-end trainable neural network RDLUF-Mix S^2 . Equipped with the proposed techniques, RDLUF-Mix S^2 achieves state-of-the-art (SOTA) performance on HSI reconstruction, as shown in Fig. 1.

2. Related Work

2.1. Deep Unfolding HSI Reconstruction

Generally, when attempting to reconstruct HSI, model-based techniques [1, 10, 15, 18, 29, 30, 35, 38, 43] adopt a Bayesian perspective and cast it as an optimization problem of maximizing the posterior probability (MAP). The optimization algorithms commonly used are HQS [11], ADMM [4], and PGD [2]. Typically, such techniques disentangle

the data fidelity and the regularization terms in the objective function, leading to an iterative procedure that alternates between solving a data subproblem and a prior subproblem.

The main idea of deep unfolding methods is that model-based iterative optimization algorithms can be implemented equivalently by a stack of recurrent DNN blocks. Such design was originally applied in deep plug-and-play methods [20, 26, 39, 41, 42], which utilize a trained denoiser to implicitly express the prior subproblem as a denoising problem. Inspired by plug-and-play, deep unfolding methods are trained end-to-end by jointly optimizing trainable denoisers for specific tasks. GAP-net [21] unfolds the generalized alternating projection algorithm and employs trained auto-encoder-based denoisers. DGSM [14] introduces an unfolding model estimation framework, which leverages the learned gaussian scale mixture prior to improve model performance. These methods typically employ the sensing matrix as the degradation matrix or a neural network is utilized to learn the degradation matrix in the data subproblem.

2.2. Methods for Exploiting Spectral and Spatial Priors

Model-based approaches often utilize manually crafted priors such as the total variation prior [38]. On the other hand, sparse-based methods [15, 17, 30] rely on the assumption that HSIs exhibit sparse representations and use ℓ_1 sparsity to regularize the solution. In addition to that, non-local based techniques [18, 35, 43] take into account the strong long-range dependency among HSI pixels to achieve more accurate results.

Previous researchers have utilized end-to-end neural networks to leverage data-driven priors, as demonstrated in [31, 32]. CNN-based methods exhibit powerful local similarity modeling capabilities. λ -net [23] reconstructs the HSIs via a two-step process. In [22], TSA-Net is proposed to exploit spatial-spectral correlation. Despite their effectiveness in some tasks, CNN-based techniques may have limitations in identifying non-local similarities as a result of their inductive biases. To address these shortcomings, transformer-based methods have been proposed, such as [5, 16]. These methods utilize multi-head self-attention mechanisms to model the long-range spatial and spectral dependency in HSIs. For instance, S-MSA in MST [5] computes dependency across spectral to generate an attention map that encodes global context implicitly. However, this approach may lead to a loss of significant spatial information related to textures and structures, which is crucial in generating high-quality HSI images.

3. Method

3.1. Problem Formulation

The degradation of CASSI system [1, 30] can be attributed to various factors, including the physical mask, dispersive prism, and 2D imaging sensor. The physical mask, denoted by $M \in \mathbb{R}^{H \times W}$, acts as a modulator for the HSI

signal $X \in \mathbb{R}^{H \times W \times N_\lambda}$, thereby enabling the representation of the n_λ^{th} wavelength of the modulated image:

$$X'_{n_\lambda} = M \odot X_{n_\lambda}, \quad (1)$$

where \odot represents the element-wise product. Consequently, the modulated HSI X' are shifted during the dispersion process, which can be expressed as:

$$X''(h, w, n_\lambda) = X'(h, w + d_{n_\lambda}, n_\lambda), \quad (2)$$

where $X'' \in \mathbb{R}^{H \times (W + d_{N_\lambda}) \times N_\lambda}$, d_{n_λ} represents the shifted distance of the n_λ^{th} wavelength. At last, the imaging sensor captures the shifted image into a 2D measurement. This process can be formulated as follow:

$$Y = \sum_{n_\lambda=1}^{N_\lambda} X''_{n_\lambda}, \quad (3)$$

the 3D HSI cube is degraded to 2D measurement $Y \in \mathbb{R}^{H \times (W + d_{N_\lambda})}$ after the sum operator, and the spatial dimensions increased as the dispersion process. As such, considering the measurement noise, the matrix-vector form of Eq. 3 can be formulated as:

$$y = \Phi x + n, \quad (4)$$

where x is the original HSI, y is the degraded measurement, Φ is the sensing matrix, generally consider it as all the degraded operators (Eq. (1, 2, 3)), and n represents the additive noise. HSI restoration aims to recover the high-quality image x from its degraded measurement y , which is typically an ill-posed problem.

Model-based methods (e.g., [1, 10, 15, 18, 29, 30, 35, 38, 43]) usually formulate HSI reconstruction as a Bayesian problem, solving Eq. (4) under a unified MAP framework:

$$\hat{x} = \underset{x}{\operatorname{argmax}} \log P(x | y) = \underset{x}{\operatorname{argmax}} \log P(y | x) + \log P(x), \quad (5)$$

where $\log P(y | x)$ and $\log P(x)$ represent the data fidelity and the regularization term, respectively. The data fidelity term is usually defined as an ℓ_2 norm, expressing Eq. (5) as the following energy function:

$$\hat{x} = \underset{x}{\operatorname{argmin}} \frac{1}{2} \|y - \Phi x\|_2^2 + \lambda J(x). \quad (6)$$

The PGD algorithm approximatively expresses Eq. (6) as an iterative convergence problem through the following iterative function:

$$\hat{x}^k = \underset{x}{\operatorname{argmin}} \frac{1}{2\rho} \|x - (\hat{x}^{k-1} - \rho \Phi^T (\Phi \hat{x}^{k-1} - y))\|_2^2 + \lambda J(x), \quad (7)$$

where \hat{x}^k refers to the output of the k -th iteration, ρ is the step size. Mathematically, the red part of the above function is a gradient descent operation and the blue part can

be solved by the proximal operator $\operatorname{prox}_{\lambda, J}$. Thus, it leads to a data subproblem and a prior subproblem, i.e., gradient descent (Eq. (8a)) and proximal mapping (Eq. (8b)):

$$v^k = \hat{x}^{k-1} - \rho \Phi^T (\Phi \hat{x}^{k-1} - y), \quad (8a)$$

$$\hat{x}^k = \operatorname{prox}_{\lambda, J}(v^k). \quad (8b)$$

The PGD algorithm iteratively updates v^k and \hat{x}^k until convergence. The model-based algorithms mainly suffer from two issues in the CASSI system. Firstly, since the sensing matrix is obtained from the equidistant lasers of different wavelengths on the sensor, it cannot reflect the device errors caused by phase aberration, distortion and alignment of the continuous spectrum. Therefore, there exist the gap between the sensing matrix and the degradation matrix that used in the data subproblem. Secondly, the handcrafted priors have to tweak parameters manually, resulting in limited representation abilities in addition to the slow reconstruction speed. To address these issues, we unfold the PGD algorithm by DNNs and integrate residual degradation learning into the gradient descent step.

3.2. Residual Degradation Learning Unfolding Framework

The whole architecture of the proposed RDLUF is presented in Fig. 2 (a), which is an unfolding framework of the PGD algorithm based on DNNs. Our RDLUF is composed of several repeated stages. Each stage contains a Residual Degradation Learning Gradient Descent (RDLGD) module and a Proximal Mapping (PM) module, corresponding to the gradient descent (Eq. (8a)) and the proximal mapping (Eq. (8b)) in an iteration step of the PGD algorithm, respectively. Additionally, there is a stage interaction between two stages to rich features and stable optimization in a spatial adaptive normalization manner.

Residual Degradation Learning Gradient Descent. In a snapshot compressive imaging system, since the sensing matrix is obtained from the equidistant lasers of different wavelengths on the sensor, it cannot reflect the device errors caused by phase aberration, distortion and alignment of the continuous spectrum. Therefore, there exists the gap between the sensing matrix Φ and the degradation matrix $\hat{\Phi}$. Previous methods proposed learning the degradation matrix using a neural network. However, it is challenging to directly model the degradation process. It is easier to optimize the residual mapping than to optimize the original, unreferenced mapping. Therefore, instead of directly learning the degradation matrix, we propose the RDLGD module to estimate the residual between the sensing matrix Φ and the degradation matrix $\hat{\Phi}$ from the compressed measurement y and the sensing matrix Φ . The RDLGD's architecture is shown in Fig. 2 (c), which is consist of several Degradation Learning Convolution Blocks (DLCBs). The DLCB is

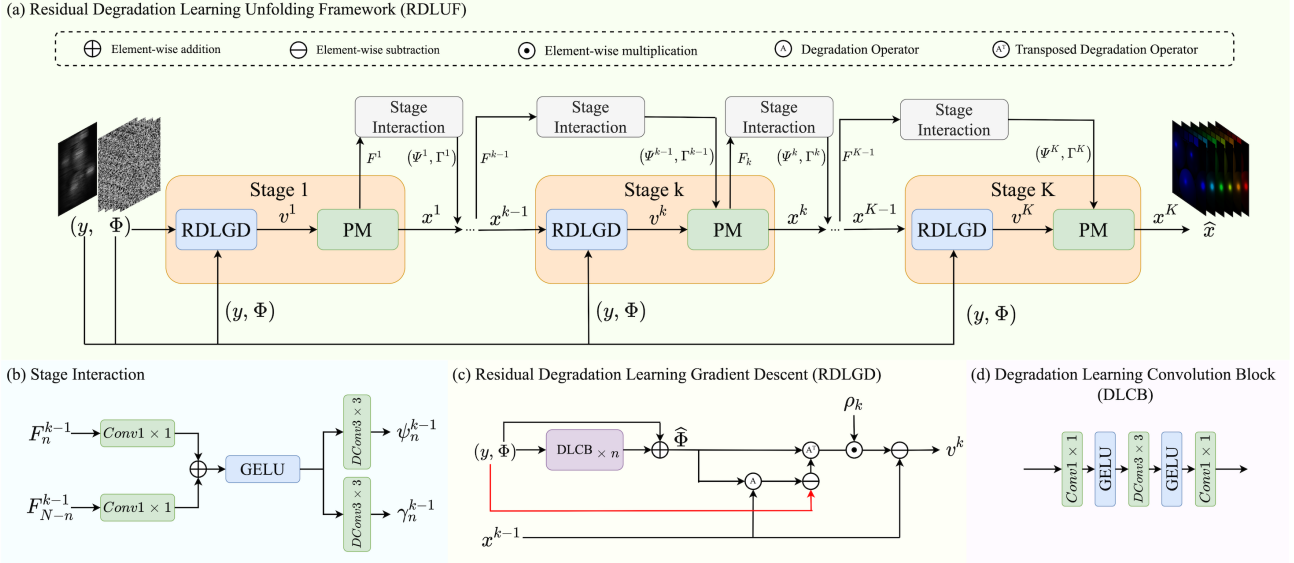


Figure 2. Our proposed RDLUF comprises K stages (iterations). $DConv$ denotes the depth-wise convolution. RDLGD calculates the degradation matrix $\hat{\Phi}$ by utilizing compressed data y and sensing matrix Φ , and executes the gradient descent with a learnable step size parameter ρ_k . There is a stage interaction between stages.

illustrated in Fig. 2 (d). The degradation matrix can be calculated as $\hat{\Phi} = \Phi + \mathcal{R}(y, \Phi)$, where \mathcal{R} represents the several cascaded DLCB, y is the compressed measurement, Φ is the sensing matrix.

Therefore, the gradient descent step in our proposed RDLUF can be expressed as:

$$v^k = \hat{x}^{k-1} - \rho^k \hat{\Phi}^\top (\hat{\Phi} \hat{x}^{k-1} - y), \quad (9)$$

where ρ is a learnable parameter, k represents the number of stage.

Proximal Mapping. For the solution of Eq. (8b), it is known that, from a Bayesian perspective, it corresponds to a denoising problem [7, 39]. In this context, we have designed the $MixS^2$ Transformer as the PM module, which effectively mixes priors across spectral and spatial, as presented in Fig. 3 (a). More details will be illustrated in the next section.

Stage Interaction. To reduce the loss of information, enrich the features of each stage and ease the network optimization procedure, we propose the stage interaction module, which generates modulation parameters from the previous stage features to normalize the current stage features in a spatial adaptive normalization manner [24, 25]. More details can be found in Appendix.

3.3. Mixing priors across Spectral and Spatial Transformer

In this section, we explain the proposed model $MixS^2$ Transformer in detail.

Network Architecture. As shown in Fig. 3 (a), the $MixS^2$ Transformer adopts a U-shaped structure consists of several basic unit $MixS^2$ blocks. There are up- and

down-sampling modules between $MixS^2$ blocks. We introduce the block interaction to reduce the loss of information caused by up- and down-sampling operations. Different scale features are interpolated to the same scale in block interaction. Firstly, the $MixS^2$ Transformer uses a $Conv3 \times 3$ to map v_k into shallow features $X_0 \in \mathbb{R}^{H \times \hat{W} \times C}$, where $\hat{W} = W + d_{N_\lambda}$. Secondly, X_0 passes through all the $MixS^2$ blocks and block interactions to be embedded into deep features $X_d \in \mathbb{R}^{H \times \hat{W} \times C}$. Finally, a $Conv3 \times 3$ operates on X_d to generate the denoised image x_k .

Mixing priors across Spectral and Spatial Block. The most important component of the $MixS^2$ Transformer is the $MixS^2$ block as shown in Fig. 3 (b), which consists of two layer normalization, a spectral self-attention branch and a lightweight inception branch in a parallel design with a bi-directional interaction, and a gated-Dconv feed-forward network [40] that is detailed in Fig. 3 (e). The up- and down-sampling modules are both a $Conv3 \times 3$ and a bi-linear interpolation with different scale factors. The details of the spectral self-attention branch, the lightweight inception branch, and the bi-directional interaction are described following.

Spectral Self-Attention Branch. The spectral self-attention branch is following [40], which $query(Q)$, $key(K)$ and $value(V)$ are embedded with a $Conv1 \times 1$ and a $DConv3 \times 3$ different from [5]. The key component of the spectral self-attention branch is S-MSA. Fig. 3 (c) shows the spectral self-attention branch. The input $X_{in} \in \mathbb{R}^{H \times W \times C}$ is first embedded, yielding $Q = W_d^Q W_p^Q X$, $K = W_d^K W_p^K X$ and $V = W_d^V W_p^V X$. Where $W_p^{(\cdot)}$ is the

fed into a spectral attention module [12] to obtain a spectral attention weight, applying to the output features of the lightweight inception module in a spectral attention manner. More details are shown in Fig. 4.

4. Experiments

4.1. Experimental Settings

We conducted both simulation and real experiments by adopting 28 wavelengths ranging from 450 nm to 650 nm for HSIs. These wavelengths were derived through spectral interpolation manipulation, inspired by the approach used in previous works [5, 14, 22].

Simulation HSI Data. In our simulation experiment, we used two HSI datasets that are widely used in the field, including CAVE and KAIST [9, 37]. The CAVE dataset comprises of 32 HSIs, with a spatial dimension of 512×512 , while the KAIST dataset has 30 HSIs with a spatial dimension of 2704×3376 . Following prior works [5, 13, 14, 16, 22], we used a real mask with a size of 256×256 during the training process. For the purpose of evaluation, we selected a total of 10 scenes from the KAIST dataset.

Real HSI Data. In our real experiment, we utilized the HSI dataset acquired through the SD-CASSI system proposed by [22]. This system captures real-world scenes using 28 wavelengths ranging from 450 to 650 nm and a 54-pixel dispersion. The spatial dimensions of the captured measurements are 660×714 .

Evaluation Metrics. The performance of HSI restoration methods will be assessed through the application of performance measures such as PSNR and SSIM [36].

Implementation Details. The RDLUF-Mix S^2 model was implemented using the PyTorch framework and trained using the Adam optimizer with hyperparameters $\beta_1 = 0.9$ and $\beta_2 = 0.999$. The training process was performed for a total of 300 epochs using the cosine annealing scheduler with a linear warm-up. The values of the learning rate and the batch size were configured as 2×10^{-4} and 1, respectively. During training, 3D HSI datasets were randomly cropped to generate patches of size $256 \times 256 \times 28$ and $660 \times 660 \times 28$, which were used as labels for the simulation and real experiments respectively. The dispersion shift steps were set to 2. Data augmentation techniques such as random flipping and rotation were employed. The objective of the model was to minimize the Charbonnier loss.

4.2. Quantitative Results

In our study, we performed a comprehensive comparative analysis of the proposed RDLUF-Mix S^2 method and SOTA HSI restoration techniques. The techniques included three model-based methods (TwIST [3], GAP-TV [38], and DeSCI [18]), as well as seven deep learning-based methods (HSSP [31], DNU [32], DGSMP [14], HDNet [13], MST [5], CST [16], and DAUHST [6]). All the techniques were trained using the same datasets and evaluated under the same settings as DGSMP [14] to ensure fair compar-

isons. The effectiveness of different methods was evaluated based on the measures of PSNR and SSIM, and the corresponding outcomes for 10 simulated scenes are demonstrated in Table 1. It is noteworthy that while CNN-based and Transformer-based techniques exhibit superior performance than model-based methods, the proposed method surpasses them all. Compared to DGSMP [14], HDNet [13], MST-L [5], CST-L* [16] and DAUHST-9stg [6], the proposed method with *9stage* achieves improvements over these methods, which are 6.94 dB, 5.23 dB, 4.39 dB, 3.45 dB and 1.21 dB on average, respectively. Additionally, the proposed method requires cheaper memory costs as shown in Fig. 1.

4.3. Qualitative Results

Simulation HSI Reconstruction. We provide a comparison of the proposed RDLUF-Mix S^2 method for HSI reconstruction, using 4 of 28 spectral channels of Scene 5, with the simulation results obtained from seven SOTA approaches. As illustrated in Fig. 5, our method produces visually smoother and cleaner textures, while preserving the spatial information of the homogeneous regions. The results demonstrate that our method is effective in generating high-quality HSIs with improved texture characteristics and spatial information preservation. Specifically, our approach leverages the spectral self-attention branch and the multi-scale convolution branch to effectively model long-range dependency and enhance the ability to capture detailed textures respectively. Furthermore, we conducted an evaluation to verify the spectral consistency of our approach by comparing the spectral density curves of the reconstructed areas to the ground truth. As illustrated in the bottom-left of Fig. 5, our method achieved the highest correlation coefficient, which highlights the effectiveness of our residual degradation learning strategy.

Real HSI Reconstruction. To conduct real experiments, we retrain our model on the CAVE [37] and KAIST [9] datasets and test on real measurements, following the settings of previous works [5, 14, 16, 22]. To simulate real measurement conditions, we introduced 11-bit shot noise during the training process. As shown in Fig. 6, we compared the reconstructed images of two real scenes (4 of 28 spectral channels of Scene 3 and Scene 4) using our RDLUF-Mix S^2 method and seven SOTA approaches. Our model achieves competitive results with SOTA methods. In Scene 3, the proposed method is able to restore more texture and detail, especially in the cactus areole area. In Scene 4, the proposed method restores the clearer right eye than other methods. Unfortunately, we find that some artifacts were introduced in the real results. This suggests that there are some challenges involved in transferring the trained network from simulated data to real data. As part of future work, we aim to analyze the factors contributing to the artifacts and devise effective measures to mitigate their impact.

Algorithms	Scene1	Scene2	Scene3	Scene4	Scene5	Scene6	Scene7	Scene8	Scene9	Scene10	Avg
TwIST [3]	25.16 0.700	23.02 0.604	21.40 0.711	30.19 0.851	21.41 0.635	20.95 0.644	22.20 0.643	21.82 0.650	22.42 0.690	22.67 0.569	23.12 0.669
GAP-TV [38]	26.82 0.754	22.89 0.610	26.31 0.802	30.65 0.852	23.64 0.703	21.85 0.663	23.76 0.688	21.98 0.655	22.63 0.682	23.10 0.584	24.36 0.669
DeSCI [18]	27.13 0.748	23.04 0.620	26.62 0.818	34.96 0.897	23.94 0.706	22.38 0.683	24.45 0.743	22.03 0.673	24.56 0.732	23.59 0.587	25.27 0.721
HSSP [31]	31.48 0.858	31.09 0.842	28.96 0.823	34.56 0.902	28.53 0.808	30.83 0.877	28.71 0.824	30.09 0.881	30.43 0.868	28.78 0.842	30.35 0.852
DNU [32]	31.72 0.863	31.13 0.846	29.99 0.845	35.34 0.908	29.03 0.833	30.87 0.887	28.99 0.839	30.13 0.885	31.03 0.876	29.14 0.849	30.74 0.863
DGSM [14]	33.26 0.915	32.09 0.898	33.06 0.925	40.54 0.964	28.86 0.882	33.08 0.937	30.74 0.886	31.55 0.923	31.66 0.911	31.44 0.925	32.63 0.917
HDNet [13]	35.14 0.935	35.67 0.940	36.03 0.943	42.30 0.969	32.69 0.946	34.46 0.952	33.67 0.926	32.48 0.941	34.89 0.942	32.38 0.937	34.97 0.943
MST-L [5]	35.40 0.941	35.87 0.944	36.51 0.953	42.27 0.973	32.77 0.947	34.80 0.955	33.66 0.925	32.67 0.948	35.39 0.949	32.50 0.941	35.18 0.948
CST-L* [16]	35.96 0.949	36.84 0.955	38.16 0.962	42.44 0.975	33.25 0.955	35.72 0.963	34.86 0.944	34.34 0.961	36.51 0.957	33.09 0.945	36.12 0.957
DAUHST-9stg [6]	37.25 0.958	39.02 0.967	41.05 0.971	46.15 0.983	35.80 0.969	37.08 0.970	37.57 0.963	35.10 0.966	40.02 0.970	34.59 0.956	38.36 0.967
Ours 3stage	36.67 0.953	38.48 0.965	40.63 0.971	46.04 0.986	34.63 0.963	36.18 0.966	35.85 0.951	34.37 0.963	38.98 0.966	33.73 0.950	37.56 0.963
Ours 5stage	37.30 0.960	39.39 0.971	42.06 0.975	46.89 0.988	35.74 0.969	37.03 0.971	37.05 0.959	35.18 0.968	40.64 0.973	34.58 0.957	38.59 0.969
Ours 7stage	37.65 0.963	40.45 0.976	43.00 0.978	47.40 0.990	36.78 0.974	37.56 0.974	38.25 0.967	35.86 0.971	41.71 0.978	34.83 0.959	39.35 0.973
Ours 9stage	37.94 0.966	40.95 0.977	43.25 0.979	47.83 0.990	37.11 0.976	37.47 0.975	38.58 0.969	35.50 0.970	41.83 0.978	35.23 0.962	39.57 0.974

Table 1. The PSNR (upper entry in each cell) in dB and SSIM (lower entry in each cell) results of the test methods on 10 scenes. RDLUF-Mix S^2 significantly surpasses other competitors.

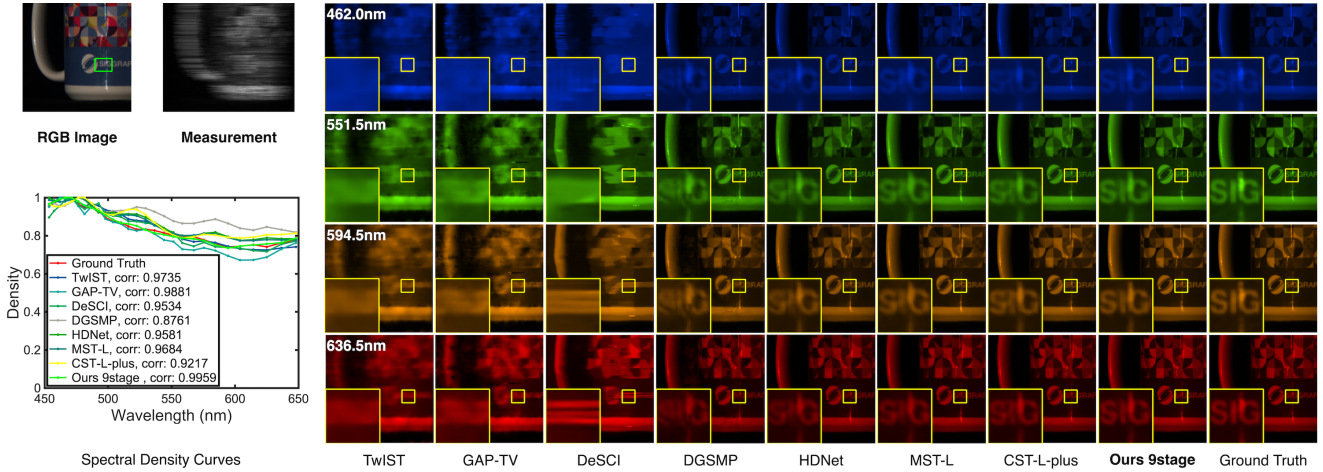


Figure 5. Comparisons of reconstructed HSIs use 4 out of 28 spectral channels in Scene 5. We evaluated 7 SOTA methods alongside the proposed approach RDLUF-Mix S^2 with 9stage. Our method’s results are most clear. The region within the green box was chosen for the analysis of the reconstructed spectra. Zoom in for a more detailed examination.

Visualization of the Residual Gradient Learning. We have visually demonstrated the learned degradation matrix and the residual between the sensing matrix and the degradation matrix in Fig. 7. It is observed that the residuals capture useful information such as object contours and minorly correct the sensing matrix.

4.4. Ablation Study

Break down ablation study. To investigate the specific impact of the different components of RDLUF-Mix S^2 on its overall performance, we conducted an ablation study,

and the detailed results are presented in Table 2. We first established a baseline model by exclusively employing the spectral branch with a plain gradient descent module, achieving results of 36.49 dB. Subsequently, applying the residual degradation learning strategy resulted in a significant improvement of 0.61 dB. Incorporating both the spectral and spatial branches lead to a further improvement of 0.20 dB. Even with few parameters, the bi-directional interaction managed to boost results by 0.11 dB. Additionally, block interaction and stage interaction yielded improve-

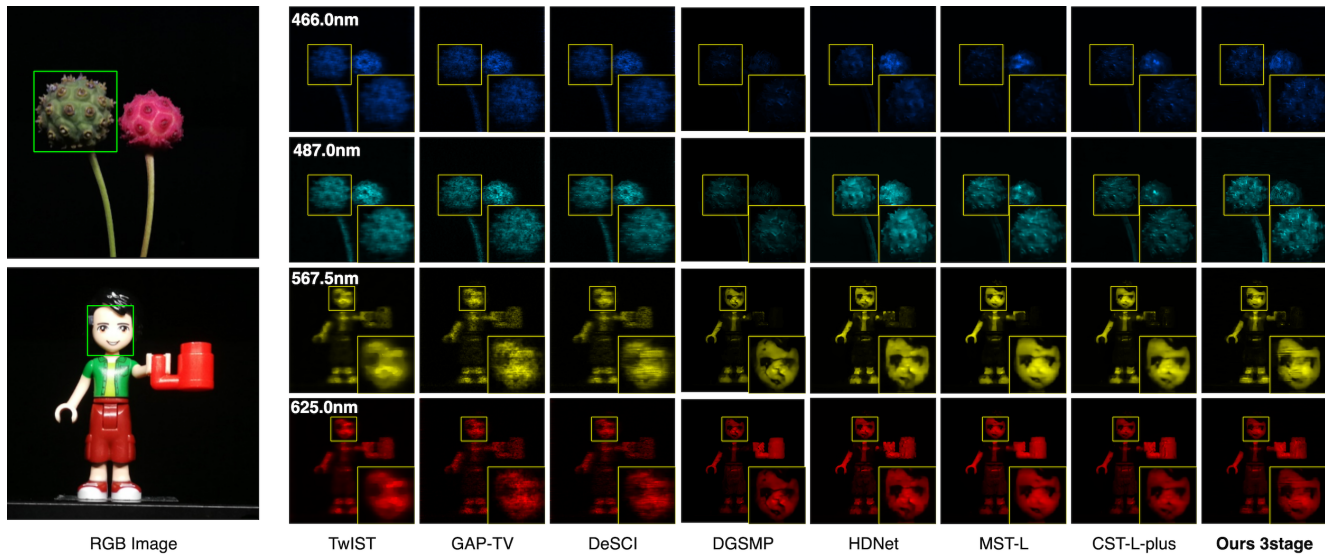


Figure 6. Real HSI reconstruction comparison of Scene 3 and Scene 4. 4 out of 28 spectra are randomly selected.

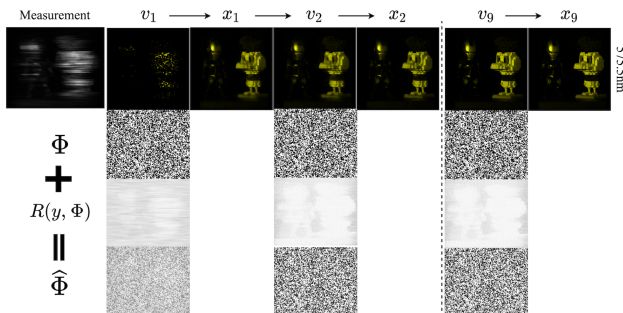


Figure 7. The results of the reconstruction, the visualizations of Φ , the residual $R(y, \Phi)$, and the corrected $\hat{\Phi}$ are presented. Please note that the visualizations are normalized and the residual response is actually small.

ments of 0.09 dB and 0.06 dB, respectively. By utilizing all components jointly, the method gained a total boost of 1.07 dB, showcasing the effectiveness of RDLUF-Mix S^2 .

		PSNR	SSIM
1	Baseline(Spectral Branch)	36.49	0.950
2	1 + Residual Degradation Learning	37.10 (+0.61)	0.955
3	2 + Spatial Branch	37.30 (+0.20)	0.958
4	3 + Bi-directional Interaction	37.41 (+0.11)	0.959
5	4 + Block Interaction	37.50 (+0.09)	0.961
6	5 + Stage Interaction	37.56 (+0.06)	0.963

Table 2. Break-down ablation studies of every component.

Number of stages. Our model shares parameters except for the first and last stages. We investigate the benefits of different numbers of stages, namely 3, 5, 7, and 9 stages. As demonstrated in Tab. 3, it can be found that the performance of the network improves with an increase in the number of stages, indicating the efficacy of the iterative network design. Based on a trade-off between reconstruction

performance and computational complexity, we find that the 7-stage approach is the optimal choice. Interestingly, we observed that sharing parameters can achieve better performance. It may suggest that a well-trained RDLGD module boosts more than multiple unshared RDLGD modules.

Number of stages	PSNR	SSIM
3	37.56	0.963
5	38.59	0.969
7	39.35	0.973
9	39.57	0.974
9*	39.03	0.971

Table 3. Ablation of number of stages. * notes all parameters is independent.

5. Conclusion and Limitation

In this paper, we first propose the RDLUF, which bridges the gap between the sensing matrix and the degradation process. Then, to strengthen the spectral-spatial representation capability in HSI, a Mix S^2 Transformer is designed via mixing priors across spectral and spatial. Finally, plugging the Mix S^2 Transformer into the RDLUF leads to an end-to-end trainable neural network RDLUF-Mix S^2 . The proposed method is demonstrated to outperform existing SOTA algorithms on simulation datasets and achieves comparable results to prior works on real datasets.

Although the proposed method achieves a large margin improvement in simulation data, the artifacts in real data suggest that transferring the trained network from simulation to real data could be a challenge. Besides, with the introduction of the convolution branch, more computational complexity is also included. Therefore, we will analyze the causes of the artifacts and make corrections and exploit some efficient implementations in future research.

References

- [1] Gonzalo R Arce, David J Brady, Lawrence Carin, Henry Arguello, and David S Kittle. Compressive coded aperture spectral imaging: An introduction. *IEEE Signal Processing Magazine*, 31(1):105–115, 2013. 1, 2, 3
- [2] Amir Beck and Marc Teboulle. A fast iterative shrinkage-thresholding algorithm for linear inverse problems. *SIAM journal on imaging sciences*, 2(1):183–202, 2009. 2
- [3] José M Bioucas-Dias and Mário AT Figueiredo. A new twist: Two-step iterative shrinkage/thresholding algorithms for image restoration. *IEEE Transactions on Image processing*, 16(12):2992–3004, 2007. 6, 7
- [4] Stephen Boyd, Neal Parikh, Eric Chu, Borja Peleato, Jonathan Eckstein, et al. Distributed optimization and statistical learning via the alternating direction method of multipliers. *Foundations and Trends® in Machine learning*, 3(1):1–122, 2011. 2
- [5] Yuanhao Cai, Jing Lin, Xiaowan Hu, Haoqian Wang, Xin Yuan, Yulun Zhang, Radu Timofte, and Luc Van Gool. Mask-guided spectral-wise transformer for efficient hyperspectral image reconstruction. In *Proceedings of the IEEE/CVF Conference on Computer Vision and Pattern Recognition*, pages 17502–17511, 2022. 1, 2, 4, 6, 7
- [6] Yuanhao Cai, Jing Lin, Haoqian Wang, Xin Yuan, Henghui Ding, Yulun Zhang, Radu Timofte, and Luc Van Gool. Degradation-aware unfolding half-shuffle transformer for spectral compressive imaging. *arXiv preprint arXiv:2205.10102*, 2022. 6, 7
- [7] Stanley H Chan, Xiran Wang, and Omar A Elgendy. Plug-and-play admm for image restoration: Fixed-point convergence and applications. *IEEE Transactions on Computational Imaging*, 3(1):84–98, 2016. 4
- [8] Qiang Chen, Qiman Wu, Jian Wang, Qinghao Hu, Tao Hu, Errui Ding, Jian Cheng, and Jingdong Wang. Mixformer: Mixing features across windows and dimensions. In *Proceedings of the IEEE/CVF Conference on Computer Vision and Pattern Recognition*, pages 5249–5259, 2022. 5
- [9] Inchang Choi, MH Kim, D Gutierrez, DS Jeon, and G Nam. High-quality hyperspectral reconstruction using a spectral prior. Technical report, 2017. 6
- [10] MA Figureido, RD Norwak, and SJ Wright. Gradient projection for sparse reconstruction: Application to compressed sensing and other inverse problem. *IEEE J. Sel. Top. Signal Process*, 1(4):586–597, 2007. 2, 3
- [11] Ran He, Wei-Shi Zheng, Tieniu Tan, and Zhenan Sun. Half-quadratic-based iterative minimization for robust sparse representation. *IEEE transactions on pattern analysis and machine intelligence*, 36(2):261–275, 2013. 2
- [12] Jie Hu, Li Shen, and Gang Sun. Squeeze-and-excitation networks. In *Proceedings of the IEEE conference on computer vision and pattern recognition*, pages 7132–7141, 2018. 6
- [13] Xiaowan Hu, Yuanhao Cai, Jing Lin, Haoqian Wang, Xin Yuan, Yulun Zhang, Radu Timofte, and Luc Van Gool. Hdnet: High-resolution dual-domain learning for spectral compressive imaging. In *Proceedings of the IEEE/CVF Conference on Computer Vision and Pattern Recognition*, pages 17542–17551, 2022. 1, 6, 7
- [14] Tao Huang, Weisheng Dong, Xin Yuan, Jinjian Wu, and Guangming Shi. Deep gaussian scale mixture prior for spectral compressive imaging. In *Proceedings of the IEEE/CVF Conference on Computer Vision and Pattern Recognition*, pages 16216–16225, 2021. 1, 2, 6, 7
- [15] David Kittle, Kerkil Choi, Ashwin Wagadarikar, and David J Brady. Multiframe image estimation for coded aperture snapshot spectral imagers. *Applied optics*, 49(36):6824–6833, 2010. 1, 2, 3
- [16] Jing Lin, Yuanhao Cai, Xiaowan Hu, Haoqian Wang, Xin Yuan, Yulun Zhang, Radu Timofte, and Luc Van Gool. Coarse-to-fine sparse transformer for hyperspectral image reconstruction. *arXiv preprint arXiv:2203.04845*, 2022. 1, 2, 6, 7
- [17] Xing Lin, Yebin Liu, Jiamin Wu, and Qionghai Dai. Spatial-spectral encoded compressive hyperspectral imaging. *ACM Transactions on Graphics (TOG)*, 33(6):1–11, 2014. 1, 2
- [18] Yang Liu, Xin Yuan, Jinli Suo, David J Brady, and Qionghai Dai. Rank minimization for snapshot compressive imaging. *IEEE transactions on pattern analysis and machine intelligence*, 41(12):2990–3006, 2018. 1, 2, 3, 6, 7
- [19] Jiawei Ma, Xiao-Yang Liu, Zheng Shou, and Xin Yuan. Deep tensor admm-net for snapshot compressive imaging. In *Proceedings of the IEEE/CVF International Conference on Computer Vision*, pages 10223–10232, 2019. 1
- [20] Tim Meinhardt, Michael Moller, Caner Hazirbas, and Daniel Cremers. Learning proximal operators: Using denoising networks for regularizing inverse imaging problems. In *Proceedings of the IEEE International Conference on Computer Vision*, pages 1781–1790, 2017. 2
- [21] Ziyi Meng, Shirin Jalali, and Xin Yuan. Gap-net for snapshot compressive imaging. *arXiv preprint arXiv:2012.08364*, 2020. 1, 2
- [22] Ziyi Meng, Jiawei Ma, and Xin Yuan. End-to-end low cost compressive spectral imaging with spatial-spectral self-attention. In *European Conference on Computer Vision*, pages 187–204. Springer, 2020. 1, 2, 6
- [23] Xin Miao, Xin Yuan, Yunchen Pu, and Vassilis Athitsos. I-net: Reconstruct hyperspectral images from a snapshot measurement. In *Proceedings of the IEEE/CVF International Conference on Computer Vision*, pages 4059–4069, 2019. 1, 2
- [24] Chong Mou, Qian Wang, and Jian Zhang. Deep generalized unfolding networks for image restoration. In *Proceedings of the IEEE/CVF Conference on Computer Vision and Pattern Recognition*, pages 17399–17410, 2022. 1, 4
- [25] Taesung Park, Ming-Yu Liu, Ting-Chun Wang, and Jun-Yan Zhu. Semantic image synthesis with spatially-adaptive normalization. In *Proceedings of the IEEE/CVF conference on computer vision and pattern recognition*, pages 2337–2346, 2019. 4
- [26] Ernest Ryu, Jialin Liu, Sicheng Wang, Xiaohan Chen, Zhangyang Wang, and Wotao Yin. Plug-and-play methods provably converge with properly trained denoisers. In *International Conference on Machine Learning*, pages 5546–5557. PMLR, 2019. 2
- [27] Christian Szegedy, Sergey Ioffe, Vincent Vanhoucke, and Alexander A Alemi. Inception-v4, inception-resnet and the

- impact of residual connections on learning. In *Thirty-first AAAI conference on artificial intelligence*, 2017. 5
- [28] Christian Szegedy, Vincent Vanhoucke, Sergey Ioffe, Jon Shlens, and Zbigniew Wojna. Rethinking the inception architecture for computer vision. In *Proceedings of the IEEE conference on computer vision and pattern recognition*, pages 2818–2826, 2016. 5
- [29] Jin Tan, Yanting Ma, Hoover Rueda, Dror Baron, and Gonzalo R Arce. Compressive hyperspectral imaging via approximate message passing. *IEEE Journal of Selected Topics in Signal Processing*, 10(2):389–401, 2015. 2, 3
- [30] Ashwin Wagadarikar, Renu John, Rebecca Willett, and David Brady. Single disperser design for coded aperture snapshot spectral imaging. *Applied optics*, 47(10):B44–B51, 2008. 1, 2, 3
- [31] Lizhi Wang, Chen Sun, Ying Fu, Min H Kim, and Hua Huang. Hyperspectral image reconstruction using a deep spatial-spectral prior. In *Proceedings of the IEEE/CVF Conference on Computer Vision and Pattern Recognition*, pages 8032–8041, 2019. 1, 2, 6, 7
- [32] Lizhi Wang, Chen Sun, Maoqing Zhang, Ying Fu, and Hua Huang. Dnu: Deep non-local unrolling for computational spectral imaging. In *Proceedings of the IEEE/CVF Conference on Computer Vision and Pattern Recognition*, pages 1661–1671, 2020. 1, 2, 6, 7
- [33] Lizhi Wang, Zhiwei Xiong, Dahua Gao, Guangming Shi, and Feng Wu. Dual-camera design for coded aperture snapshot spectral imaging. *Applied optics*, 54(4):848–858, 2015. 1
- [34] Lizhi Wang, Zhiwei Xiong, Dahua Gao, Guangming Shi, Wenjun Zeng, and Feng Wu. High-speed hyperspectral video acquisition with a dual-camera architecture. In *Proceedings of the IEEE Conference on Computer Vision and Pattern Recognition*, pages 4942–4950, 2015. 1
- [35] Lizhi Wang, Zhiwei Xiong, Guangming Shi, Feng Wu, and Wenjun Zeng. Adaptive nonlocal sparse representation for dual-camera compressive hyperspectral imaging. *IEEE transactions on pattern analysis and machine intelligence*, 39(10):2104–2111, 2016. 1, 2, 3
- [36] Zhou Wang, Alan C Bovik, Hamid R Sheikh, and Eero P Simoncelli. Image quality assessment: from error visibility to structural similarity. *IEEE transactions on image processing*, 13(4):600–612, 2004. 6
- [37] Fumihito Yasuma, Tomoo Mitsunaga, Daisuke Iso, and Shree K Nayar. Generalized assorted pixel camera: post-capture control of resolution, dynamic range, and spectrum. *IEEE transactions on image processing*, 19(9):2241–2253, 2010. 6
- [38] Xin Yuan. Generalized alternating projection based total variation minimization for compressive sensing. In *2016 IEEE International Conference on Image Processing (ICIP)*, pages 2539–2543. IEEE, 2016. 1, 2, 3, 6, 7
- [39] Xin Yuan, Yang Liu, Jinli Suo, and Qionghai Dai. Plug-and-play algorithms for large-scale snapshot compressive imaging. In *Proceedings of the IEEE/CVF Conference on Computer Vision and Pattern Recognition*, pages 1447–1457, 2020. 2, 4
- [40] Syed Waqas Zamir, Aditya Arora, Salman Khan, Munawar Hayat, Fahad Shahbaz Khan, and Ming-Hsuan Yang. Restormer: Efficient transformer for high-resolution image restoration. In *Proceedings of the IEEE/CVF Conference on Computer Vision and Pattern Recognition*, pages 5728–5739, 2022. 4
- [41] Kai Zhang, Wangmeng Zuo, Shuhang Gu, and Lei Zhang. Learning deep cnn denoiser prior for image restoration. In *Proceedings of the IEEE conference on computer vision and pattern recognition*, pages 3929–3938, 2017. 2
- [42] Kai Zhang, Wangmeng Zuo, and Lei Zhang. Deep plug-and-play super-resolution for arbitrary blur kernels. In *Proceedings of the IEEE/CVF Conference on Computer Vision and Pattern Recognition*, pages 1671–1681, 2019. 2
- [43] Shipeng Zhang, Lizhi Wang, Ying Fu, Xiaoming Zhong, and Hua Huang. Computational hyperspectral imaging based on dimension-discriminative low-rank tensor recovery. In *Proceedings of the IEEE/CVF International Conference on Computer Vision*, pages 10183–10192, 2019. 1, 2, 3
- [44] Xuanyu Zhang, Yongbing Zhang, Ruiqin Xiong, Qilin Sun, and Jian Zhang. Herosnet: Hyperspectral explicable reconstruction and optimal sampling deep network for snapshot compressive imaging. In *Proceedings of the IEEE/CVF Conference on Computer Vision and Pattern Recognition*, pages 17532–17541, 2022. 1